Liquid Crystal Microfluidics for Tunable Flow Shaping

Anupam Sengupta,[1,*] Uroš Tkalec,[1,2] Miha Ravnik,[3,4,2] Julia M. Yeomans,[3] Christian Bahr,[1] and Stephan Herminghaus[1]

[1]*Max Planck Institute for Dynamics and Self-Organization (MPIDS), 37077 Göttingen, Germany*
[2]*Center of Excellence NAMASTE, Jamova 39, 1000 Ljubljana, Slovenia*
[3]*Rudolf Peierls Centre for Theoretical Physics, University of Oxford, 1 Keble Road, Oxford OX1 3NP, United Kingdom*
[4]*Faculty of Mathematics and Physics, University of Ljubljana, Jadranska 19, 1000 Ljubljana, Slovenia*

(Received 30 August 2012; published 25 January 2013)

We explore the flow of a nematic liquid crystal in microfluidic channels with a rectangular cross section through experiments and numerical modeling. The flow profile and the liquid crystal orientational profile show three distinct regimes of weak, medium, and strong flow as the driving pressure is varied. These are identified by comparing polarizing optical microscopy experiments and numerical solutions of the nematofluidic equations of motion. The relative stability of the regimes is related to the de Gennes characteristic shear-flow lengths e_1 and e_2, together with the channel's aspect ratio w/d. Finally, we show that the liquid crystalline microfluidic flow can be fully steered from left to right of a simple microchannel by applying transverse temperature gradients.

DOI: 10.1103/PhysRevLett.110.048303 PACS numbers: 47.57.Lj, 61.30.Jf

Microfluidics manipulates fluids in confined geometries, typically channels with dimensions of tens of micrometers [1]. It has emerged as an efficient tool for a wide spectrum of applications: from miniaturization of conventional fluidic elements, such as pumps, valves, and membranes, to enhanced throughput for analysis, mixing, transport and particle separation in medicine and biology [2]. Such applications rely on modulation of the flow achieved through innovative lithographic architectures, and employ isotropic fluids which furnish Poiseuille-like flow profiles [3,4]. Explorations beyond this Poiseuille-profile-determined regime could open new microfluidic phenomena and applications [5]. Although experimental investigations of complex fluids in microfluidic confinements have been initiated [6–8], understanding of their dynamics is mostly limited to numerical studies [9–13].

Investigations on liquid crystals (LCs) as a natural choice for an anisotropic replacement of the isotropic fluids have been directed mostly towards effects mediated by topological defects [14–18]. Combined with the functionality of dispersed particles, advanced optics, field manipulation, and microstructuring, nematic liquid crystals (NLCs) have grown to beyond-the-display materials, as they are capable of colloidal self-assembly [14], state imprinted memory effects [15], low concentration sensing [19], and reconfigurable directional interactions [20]. The distinctive edge of NLCs over other materials lies in their microscopic anisotropy due to the orientational ordering [21]. This anisotropy is imprinted also on the flow of NLCs via a coupling between the orientational order and the flow, a mechanism known as backflow [22]. Most of the existing literature focuses on the flow of nematic LCs within very wide channels—or slits (cells), as relevant in display applications. However, in any microfluidic application, one encounters channel flows where the width and depth of the channels are comparable. Only very recently, experiments on backflow dynamics are starting to emerge in microfluidic setups, reporting on flow induced transitions [23], effects of molecular pretilt at confining surfaces [24], nematic textures in untreated channels [25], nematic flows driven by thermoexpansion [26], and electrically or mechanically modulated microflows [27,28].

In this Letter, we demonstrate shaping of flow profiles in microfluidic channels by affecting the orientation and the order of nematic fluids. The otherwise Poiseuille profile is transformed into three general complex non-Poiseuille multistream profiles in a simple rectangular homeotropic microchannel: (i) in the weak-flow regime the nematic flow and orientational order are only weakly coupled and are mostly determined by the surface, (ii) in the medium-flow regime largest variability in both flow and nematic profile is observed, caused by the intricate backflow coupling, and (iii) strong flow is determined by flow alignment of the LC molecules. We show that the dynamics can be characterized by the de Gennes characteristic shear-flow lengths e_1 and e_2 which, together with the channel's aspect ratio w/d, control the relative stability of the flow regimes. In addition, we show that the pressure-driven flow profile can be easily and effectively manipulated by externally applied temperature gradients via changes in the nematic degree of order.

We observed the flow of the nematic LC pentyl-cyanobiphenyl (5CB) through linear microchannels with a rectangular cross section. The channels were fabricated out of polydimethylsiloxane (PDMS, Sylgard 184, Dow Corning) reliefs and glass substrates following standard soft lithography procedures [29]. Subsequent treatment with 0.1 wt% aqueous solution of *N*-dimethyl-*n*-octadecyl-3-aminopropyl-trimethoxysilyl chloride (DMOAP) was applied to induce strong homeotropic surface anchoring [29]. The channel width w was set to 100 μm, while the

depth d varied between 5 and 30 μm. The inlet tube was connected to a gas-tight microliter syringe filled with 5CB and the outlet tube was immersed in a 5CB sink. The syringe was driven by a gear pump (neMESYS, Cetoni) with a flow rate precision of 1 nl/h. The flow regimes were studied by polarizing optical microscopy (POM), fluorescence confocal polarizing microscopy (FCPM), and particle tracking velocimetry [30]. For FCPM, 5CB was doped with 0.01 wt% of the fluorescent dye Nile Red (Sigma Aldrich). We show stationary flow regimes; however, if using time-dependent flow driving, time-dependent and variable director and flow states are also generated.

Numerical modeling based on solving the Beris-Edwards model of nematofluidics with the hybrid lattice Boltzmann algorithm complements the experiments [10]. Time-evolution equations for the nematic order parameter tensor Q_{ij} and fluid velocity u_i are:

$$(\partial_t + u_k\partial_k)Q_{ij} - S_{ij} = \Gamma H_{ij}, \tag{1}$$

$$\rho(\partial_t + u_k\partial_k)u_i = \partial_j\Pi_{ij} + \eta\partial_j[\partial_i u_j + \partial_j u_i + (1 - 3\partial_\rho P)\partial_k u_k\delta_{ij}], \tag{2}$$

where ∂_t is a derivative in time t, ∂_i is a derivative in the Cartesian spatial coordinate x, y, z, Γ is a rotational diffusion coefficient, η is the viscosity, and summation over repeated indices is assumed. The relaxation to equilibrium of Q_{ij} is determined by the molecular field H_{ij}, which relates to the nematic (Landau-de Gennes) free energy $\mathcal{F}$, $H_{ij} = -\frac{\delta\mathcal{F}}{\delta Q_{ij}} + (\delta_{ij}/3)\mathrm{Tr}\frac{\delta\mathcal{F}}{\delta Q_{kl}}$, where

$$\mathcal{F} = L(\partial_k Q_{ij})^2/2 + AQ_{ij}Q_{ji}/2 + BQ_{ij}Q_{jk}Q_{ki}/3 + C(Q_{ij}Q_{ji})^2/4, \tag{3}$$

L is a single elastic constant, and A, B, C are material constants. Flow driving is achieved by a body force implemented according to Guo *et al.* [31]. For more details about the model and definition of the stress tensor Π_{ij}, generalized advection S_{ij}, and effective compressibility P refer to Ref. [10]. The simulations are performed in a rectangular slice through the microchannel with a cubic lattice; typically $4 \times 400 \times 100$ mesh points. Along the channel (x), we assume periodic boundary conditions for both Q_{ij} and u_i, whereas at the channel walls we take no-slip boundary conditions for u_i (standard bounceback) and fixed homeotropic boundary conditions for Q_{ij}. The following are the values of material parameters used: $L = 40$ pN, $A = -0.172$ MJ/m^3, $B = -2.12$ MJ/m^3, $C = 1.73$ MJ/m^3, flow aligning regime $\xi = 1$, $P_0 = 100$ kPa, $\Gamma = 7.29$ Pas, the mesh resolution $\Delta = 10$ nm, time step $\Delta t = 0.34$ μs, and body force of 0.001, 0.01, and 0.1 for the weak-, medium-, and strong-flow regime, respectively. Fluorescence confocal signal intensity I is calculated from the local director n_i and laser polarization P_i as $I \propto (n_i P_i)^4$ and POM micrographs are calculated with the Jones 2×2 matrix formalism [32].

The scheme of our microfluidic setup is presented in Fig. 1(a). In the absence of flow, such microchannels support multiple nematic configurations, either stable or metastable, depending on the topological structure of the defects in the corners of the channels. Experimentally, always a single stable structure emerges [see Figs. 1(b) and 1(c)], which indeed has the lowest total free energy, as confirmed by numerical modeling. This equilibrium no-flow structure proves important upon starting the flow, as it registers the initial state for the subsequent dynamics. We should note that a structure as shown in Fig. 1 is obtained only for rectangular cross sections; for channels with a square or circular cross section, an escaped director configuration [33], in which the director aligns parallel to the channel axis in the middle of the channel, would be expected.

Upon starting the flow, three distinct flow regimes are observed, which we categorize into (A) weak, (B) medium, and (C) strong, as presented in Fig. 2. In the weak-flow regime, the nematic structure remains similar to the no-flow configuration, with the director being along the z direction in the major part of the channel. The microchannel is dark between crossed polarizers [Fig. 2A(a)] and gives a low FCPM signal [Fig. 2A(b)] at both xy and yz planes, except close to the walls due to the conflicting surface anchoring. Corresponding numerical modeling shows good agreement with experiments, and reveals nematic distortion only in the yz plane [Fig. 2A(c)]. Low-flow speeds (≤ 11 μm/s) and hence low Ericksen numbers (Er ≈ 1) show the dominance of LC elasticity over the backflow (we use the term "backflow" as an acronym for the coupling between flow and director orientation).

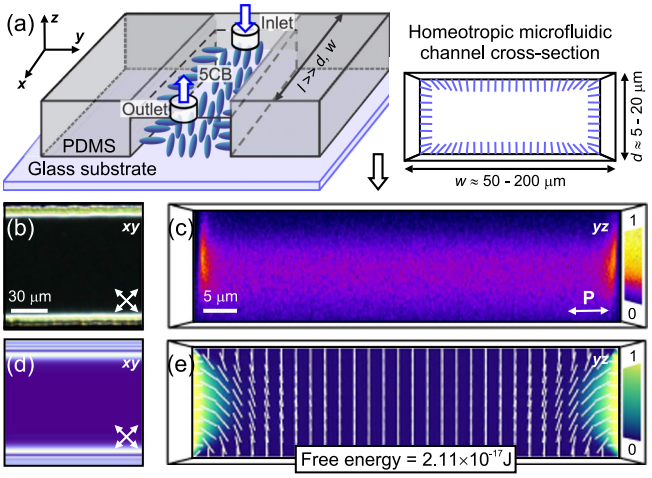

FIG. 1 (color online). No-flow nematic profile in a rectangular homeotropic channel. (a) Scheme of the microfluidic setup. Experimental (b) POM and (c) FCPM micrographs of a 100 μm $\times$ 10 μm channel and corresponding numerically modeled (d) POM and (e) FCPM images with director and total free energy.

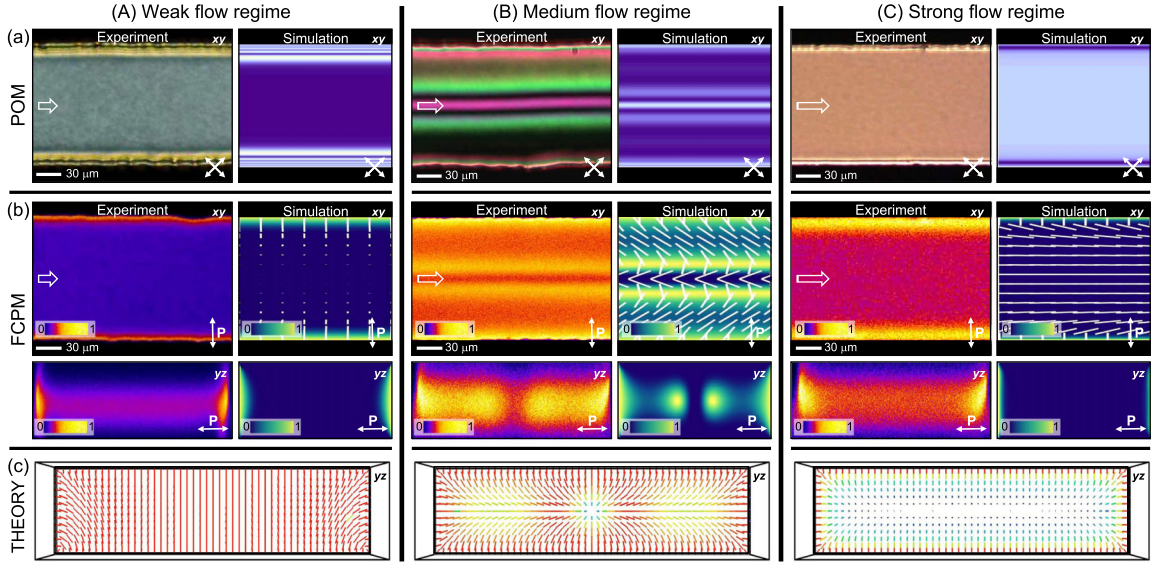

FIG. 2 (color online). Three basic flow regimes in the homeotropic microchannel: (A) weak flow, (B) medium flow, and (C) strong flow. Results show (a) experimental and calculated POM micrographs in the xy plane and (b) experimental and calculated FCPM micrographs in the xy and yz planes including the director configuration at the half-depth of the channel. 0 and 1 respectively indicate the nematic director orthogonal and parallel to the excitation laser polarization. (c) The full director profile calculated across the channel cross section for the three regimes. Blue color, or shorter lines, indicate out-of-plane director orientation, whereas red color, or longer lines, correspond to in-plane director orientation. Experiments were performed in a 16 μm deep channel.

In the medium-flow regime (flow speeds $v \approx 30$ μm/s, Fig. 2B), we observe complex flow rheology, caused by the competition between the nematic elasticity and the backflow. In the center of the channels, symmetrical changes emerge in the birefringence due to locally high shear rates as imposed by the no-slip at the walls and flow driving in the centers of the channels [Figs. 2B(a),(b)]. From numerical simulations, they are found to represent complex bend and splay deformations of the director, as shown in Fig. 2B(c). More specifically, in the central and two symmetric side regions, the backflow mechanism [34] realigns the director in the direction along the channel to optimize the coupling between the local shear and the nematic distortions.

In the high-flow regime (flow speeds $v \approx 100$ μm/s, Fig. 2C), the nematic profile evolves into a flow-aligned state, with the director primarily along the channel direction Fig. 2C(a), as resolved by confocal imaging [Fig. 2C(b)] and in good qualitative agreement with the numerical calculations Fig. 2C(c). Interestingly, this observed high-flow-regime nematic profile is analogous to the escaped radial nematic profile, typically observed in nematic-filled capillaries; however, now with a bend angle which depends on the flow profile.

The flow profiles of the three regimes are presented in Figs. 3(a)–3(c), as measured by particle tracking and numerical modeling. In weak flows, due to weak backflow coupling, the nematic flow profile is similar to those of isotropic fluids, which in rectangular channels can be expressed as a Fourier sum of sin functions along z direction and appropriately weighted cosh functions along the y direction [4]. However, in the medium-flow regime, the backflow mechanism emerges significantly. The flow profile evolves into a *two-stream* flow, identified by a lower velocity region at the channel center which is surrounded symmetrically by higher velocity regions. Experimentally, the maximum speed in a 7 μm deep channel (aspect ratio 14:1) is measured to be 6% higher than the velocity at the channel center. Within deeper channels, this difference is more pronounced: Numerical simulations for an aspect ratio of 4:1 yield a speed difference of 12%. On overlaying the profile to the corresponding director field (Fig. 2B), the lower velocity maps to the splay-bend deformation region, whereas the higher velocity regions correspond to regions with the director partially aligned along the flow. Effectively, it is the spatial variation of the apparent viscosity from the backflow mechanism that is responsible for this two-stream flow profile. At strong flows, the flow profile becomes again similar to that of isotropic fluids, because the director field is homogeneous except for close to the surfaces. We should note that the effective viscosity in the strong-flow regime is smaller than in the weak-flow regime, because of the different mean orientation of the director relative to the flow.

The regimes discussed are stable over a range of flow speeds which depend on the channel depth d [Figs. 3(d)–3(f)]. For example in the 7 μm shallow channel, the weak regime persists up-to flow speeds of ≈ 40 μm/s, whereas in the 35 μm deep channel the regime destabilizes at a considerably lower speed of

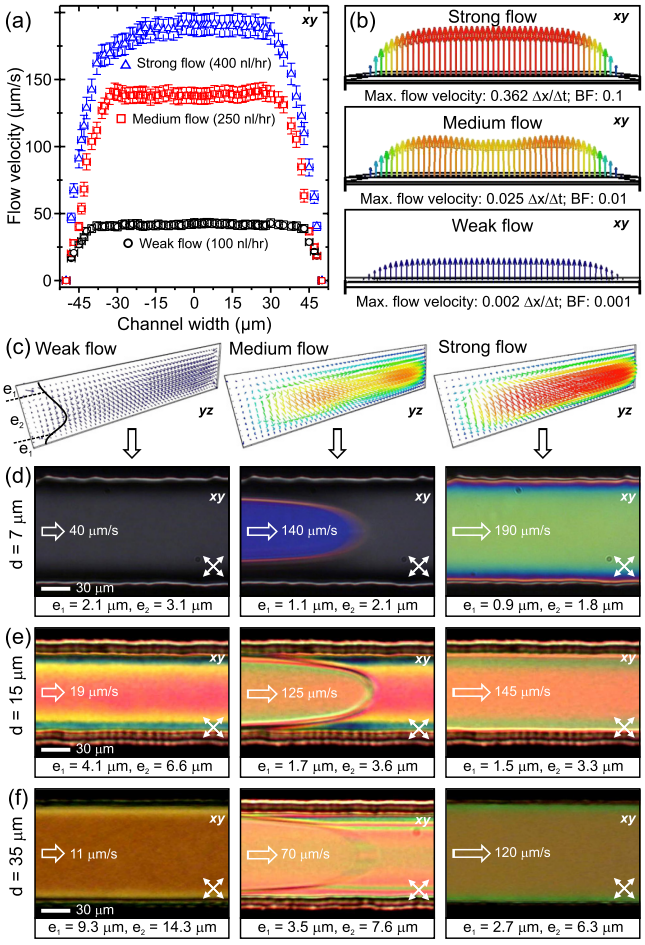

FIG. 3 (color online). Flow profiles of the weak-, medium-, and strong-flow regimes. (a) Experimental-flow profiles at the half-depth of the channel. One stream flow is dominant in the low and high-flow regimes. Two-stream flow is observed in the medium-flow regime. (b) Flow profiles at half-depth for the three regimes obtained from numerical modeling and (c) the same flow profiles across the full channel cross section. (d)–(f) POM micrographs representing the evolution of the flow regimes in channels with three different depths. Note the appearance of the parabolic front upon increasing the flow. e_1 and e_2 values are calculated from experimentally measured average shear rates.

≈ 10 μm/s. Moreover, a flow speed of ≈ 120 μm/s in the deeper channel is sufficient for the director to align parallel with the flow, whereas only partial alignment is observed in the shallow channel, even at flow speeds >200 μm/s. These differences can be captured by the de Gennes shear flow characteristic lengths $e_1 \propto \sqrt{Ld/2\eta v}$ and $e_2 \propto \sqrt[3]{de_1^2}$ [21], which measure the widths of the transition layers over which the director is reoriented by the local shear flow near the walls and in the centre of the channel respectively. For a given channel depth d, as flow speed increases, e_1 and e_2 decrease. When the sum $2e_1 + e_2$ becomes comparable to d, the transition to the flow aligned state occurs on increasing the flow speed further. Thereafter, one has only the transition layers at the channel walls, whereas at the center the director is aligned along the flow. Using the estimate $L/(2\eta) = 25 \times 10^{-12}$ m^2 s^{-1}, in the shallow channel [Fig. 3(d)], $e_1 = 2.1$ μm and $e_2 = 3.1$ μm are obtained from the measured average shear rate $s = v/(0.5d)$ and maximum flow speed $v = 40$ μm/s. These sum up to the full depth of the channel, $2e_1 + e_2 \approx d$, and mark the transition. In contrast, in the deep channel [Fig. 3(f)], a similar condition is achieved only at $v \leq 11$ μm/s.

Finally, we demonstrate another possibility to tune the flow of nematic fluids: A transverse temperature gradient, applied across the microfluidic channel, was used to controllably steer the flow profile. The gradient was controlled using a dc voltage applied across a heating element placed parallel to one of the side walls of the channel. The opposite wall was left at room temperature. In isotropic fluids (e.g., water or oil), applying the temperature gradient is a standard way to introduce an asymmetry in the flow profile by affecting primarily the viscosity of the fluid [4]. Typically, this effect is small in isotropic fluids and changes mostly the magnitude and only weakly the profile of the flow (see inset in Fig. 4). However, in the nematic fluid, the temperature gradient leads to a gradient in the nematic ordering which in turn affects the backflow and induces a strong bias in the flow profile, as shown in Fig. 4. A distinct flow stream emerges at the higher temperature side of the channel, which is by a factor of ≈ 2 larger than the flow velocity on the (symmetric) opposite side of the channel. Further, the position and magnitude of this flow

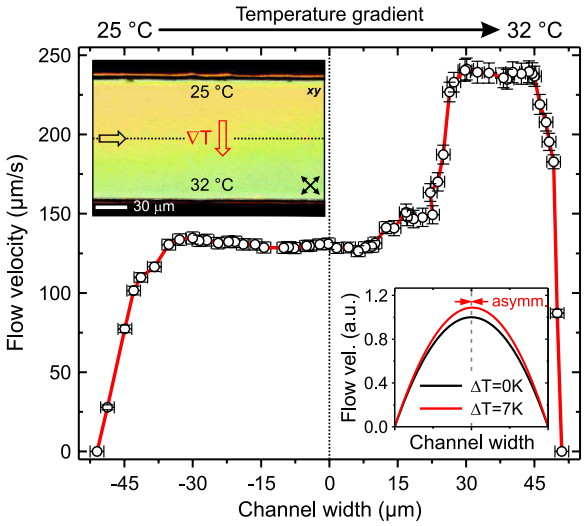

FIG. 4 (color online). Steering of the microflow profile by a transverse temperature gradient. The opposite transverse channel walls are temperature stabilized at 25 °C and 32 °C. The top-left inset shows a top-view polarization micrograph of the channel. Channel depth is 10 μm. For comparison, the bottom-right inset shows the typical change of the Poiseuille flow profile in an isotropic fluid upon applying an equal temperature gradient, causing changes in the viscosity of $\alpha_\eta = \Delta\eta/\eta = -0.175$ (see Ref. [4]).

stream can be tuned by varying the temperature gradient. Similar flow steering can also be achieved in the medium- and weak-flow regimes [30], and indicates interesting possible applications for sorting and colloidal manipulation based on nematic microfluidics.

In conclusion, the backflow mechanism in nematic fluids proves to be a strong route to sensitively tune complex microflows. Three flow regimes—weak, medium, and strong—are observed in rectangular microchannels with uniform homeotropic boundary conditions, each characterized by distinct director and flow profiles. A multipeak flow distribution is achieved in the channels without any morphological patterning or advanced channel design. Asymmetric flow streams are generated and precisely steered by transverse temperature gradients, indicating high potential for diverse flow shaping. The dynamically regulated nematic flow profiles observed indicate interesting applications beyond the capabilities of isotropic microfluidics, including flow mixing, large-scale transport, high-throughput separation of colloidal inclusions, and active-response optical detection of pressure changes within microfluidic networks.

This work was supported by EU Marie Curie grants HIERARCHY, ACTOIDS, FREEFLUID, EU-SLO Centre of Excellence NAMASTE, and Max Planck Society.

*anupam.sengupta@ds.mpg.de

[1] G. M. Whitesides, Nature (London) **442**, 368 (2006).
[2] D. J. Beebe, G. A. Mensing, and G. M. Walker, Annu. Rev. Biomed. Eng. **4**, 261 (2002); H. A. Stone, A. D. Stroock, and A. Ajdari, Annu. Rev. Fluid Mech. **36**, 381 (2004).
[3] T. M. Squires and S. R. Quake, Rev. Mod. Phys. **77**, 977 (2005).
[4] H. Bruus, *Theoretical Microfluidics* (Oxford University Press, Oxford, 2008).
[5] D. Psaltis, S. R. Quake, and C. Yang, Nature (London) **442**, 381 (2006); J. Leach, H. Mushfique, R. di Leonardo, M. Padgett, and J. Cooper, Lab Chip **6**, 735 (2006); A. Sengupta, S. Herminghaus, and Ch. Bahr, Appl. Phys. Lett. **101**, 164101 (2012).
[6] T. Pfohl, F. Mugele, R. Seemann, and S. Herminghaus, ChemPhysChem **4**, 1291 (2003); P. Nghe, E. Terriac, M. Schneider, Z. Z. Li, M. Cloitre, B. Abecassisa, and P. Tabeling, Lab Chip **11**, 788 (2011).
[7] M. C. Choi, T. Pfohl, Z. Wen, Y. Li, M. W. Kim, J. N. Israelachvili, and C. R. Safinya, Proc. Natl. Acad. Sci. U.S.A. **101**, 17340 (2004); S. Shojaei-Zadeh and S. L. Anna, Langmuir **22**, 9986 (2006).
[8] B. D. Hamlington, B. Steinhaus, J. J. Feng, D. Link, M. J. Shelley, and A. Q. Shen, Liq. Cryst. **34**, 861 (2007).
[9] J. Feng and L. G. Leal, Phys. Fluids **11**, 2821 (1999).
[10] C. Denniston, E. Orlandini, and J. M. Yeomans, Comput. Theor. Polym. Sci. **11**, 389 (2001); C. Denniston, D. Marenduzzo, E. Orlandini, and J. M. Yeomans, Phil. Trans. R. Soc. A **362**, 1745 (2004).
[11] J. Quintas Carou, B. R. Duffy, N. J. Mottram, and S. K. Wilson, Phys. Fluids **18**, 027105 (2006).
[12] J. P. Hernandez-Ortiz, B. T. Gettelfinger, J. Moreno-Razo, and J. J. de Pablo, J. Chem. Phys. **134**, 134905 (2011).
[13] L. Giomi, L. Mahadevan, B. Chakraborty, and M. F. Hagan, Phys. Rev. Lett. **106**, 218101 (2011); L. Giomi and M. C. Marchetti, Soft Matter **8**, 129 (2012).
[14] P. Poulin, H. Stark, T. C. Lubensky, and D. A. Weitz, Science **275**, 1770 (1997); I. Muševič, M. Škarabot, U. Tkalec, M. Ravnik, and S. Žumer, Science **313**, 954 (2006).
[15] T. Araki, M. Buscaglia, T. Bellini, and H. Tanaka, Nat. Mater. **10**, 303 (2011).
[16] G. Toth, C. Denniston, and J. M. Yeomans, Phys. Rev. Lett. **88**, 105504 (2002); C. Blanc, D. Svenšek, S. Žumer, and M. Nobili, Phys. Rev. Lett. **95**, 097802 (2005).
[17] O. D. Lavrentovich, I. Lazo, and O. P. Pishnyak, Nature (London) **467**, 947 (2010); O. P. Pishnyak, S. V. Shiyanovskii, and O. D. Lavrentovich, Phys. Rev. Lett. **106**, 047801 (2011).
[18] J. S. Lintuvuori, K. Stratford, M. E. Cates, and D. Marenduzzo, Phys. Rev. Lett. **105**, 178302 (2010).
[19] I.-H. Lin, D. S. Miller, P. J. Bertics, C. J. Murphy, J. J. de Pablo, and N. L. Abbot, Science **332**, 1297 (2011).
[20] T. Lopez-Leon, V. Koning, K. B. S. Devaiah, V. Vitelli, and A. Fernandez-Nieves, Nat. Phys.**7**, 391 (2011).
[21] P. G. de Gennes and J. Prost, *The Physics of Liquid Crystals* (Oxford Science Publications, Oxford, 1993).
[22] J. L. Ericksen, Arch. Ration. Mech. Anal. **4**, 231 (1959); F. M. Leslie and Q. J. Mech, Q. J. Mech. Appl. Math. **19**, 357 (1966); F. M. Leslie, Arch. Ration. Mech. Anal. **28**, 265 (1968).
[23] S. A. Jewell, S. L. Cornford, F. Yang, P. S. Cann, and J. R. Sambles, Phys. Rev. E **80**, 041706 (2009); C. J. Holmes, S. L. Cornford, and J. R. Sambles, Appl. Phys. Lett. **95**, 171114 (2009).
[24] C. J. Holmes, S. L. Cornford, and J. R. Sambles, Phys. Rev. Lett. **104**, 248301 (2010).
[25] A. Sengupta, U. Tkalec, and Ch. Bahr, Soft Matter **7**, 6542 (2011).
[26] Y.-K. Kim, B. Senyuk, and O. D. Lavrentovich, Nat. Commun. **3**, 1133 (2012).
[27] Y.-J. Na, T.-Y. Yoon, S. Park, B. Lee, and S.-D. Lee, ChemPhysChem **11**, 101 (2010).
[28] J. G. Cuennet, A. E. Vasdekis, L. De Sio, and D. Psaltis, Nat. Photonics **5**, 234 (2011).
[29] A. Sengupta, B. Schulz, E. Ouskova, and Ch. Bahr, Microfluid. Nanofluid. **13**, 941 (2012).
[30] See Supplemental Material at http://link.aps.org/supplemental/10.1103/PhysRevLett.110.048303 for experimental details of the particle tracking velocimetry and for information about the effect of a transverse temperature gradient in the weak- and medium-flow regimes.
[31] Z. Guo, C. Zheng, and B. Shi, Phys. Rev. E **65**, 046308 (2002).
[32] R. Ondris-Crawford, E. P. Boyko, B. G. Wagner, J. H. Erdmann, S. Žumer, and J. W. Doane, J. Appl. Phys. **69**, 6380 (1991).
[33] P. E. Cladis and M. Kléman, J. Phys. (Paris) **33**, 591 (1972).
[34] A. N. Beris and B. J. Edwards, *Thermodynamics of Flowing Systems* (Oxford University Press, Oxford, 1994).